RSC Advances

ROYAL SOCIETY OF CHEMISTRY

www.rsc.org/advances

Table of Content

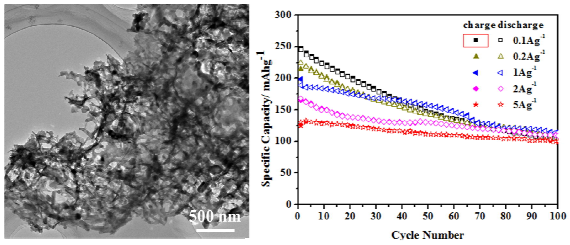

Interpenetrating V_2O_5 nanosheets/CNTs nanocomposite was fabricated by freeze-drying method which performs excellent electrochemical properties for fast lithium storage.

RSC Advances

RSCPublishing

ARTICLE

Interpenetrating network of V_2O_5 nanosheets/carbon nanotubes nanocomposite for fast lithium storage

Cite this: DOI: 10.1039/xoxxoooooox

Zhaolong Li[a], Quanyao Zhu[a,#], Shengnan Huang[a], Shanshan Jiang[a], Shan Lu[a], Wen Chen[a,*] and Galina S. Zakharova[b]

Received ooth January 2014,
Accepted ooth January 2014

DOI: 10.1039/xoxxoooooox

www.rsc.org/

Rapid charge and discharge cathode materials for lithium ion batteries (LIBs) have been commonly researched for the development of electrical mobility applications. Here, interpenetrating network vanadium pentoxide (V_2O_5) nanosheets/carbon nanotubes (CNTs) nanocomposite was fabricated by freeze-drying process. The field emission scanning electron microscopy (FESEM) and transmission electron microscopy (TEM) tests exhibited that the CNTs and V_2O_5 nanosheets form an interpenetrating network structure. The X-ray diffraction (XRD) and X-ray photoelectron spectroscopy (XPS) analyses confirmed that the V_2O_5 nanosheets exhibit orthorhombic crystal structure and mixture element states in the nanocomposite. The electrochemical properties of the V_2O_5 nanosheets/CNTs nanocomposite were studied by cyclic voltammetry (CV), electrochemical impedance spectroscopy (EIS) and galvanostatic charge-discharge measurements. The results indicated that the V_2O_5 nanosheets/CNTs nanocomposite exhibits high specific capacity and good cycling stability. The initial specific capacity of the V_2O_5 nanosheets/CNTs nanocomposite is 130.7 mAh•g^{-1} as the current density up to 5.0 $Ag^{-1}$and remains 100.1 $mAhg^{-1}$ after 100 cycles.

Introduction

Lithium-ion batteries (LIBs) have become the dominant power sources for cell phones, digital cameras, laptops etc., due to their suitable energy density, high-efficient and environmentally friendly.[1] However, LIBs with high power density for fast charge-discharge rate are urgently required to meet the future demand of hybrid vehicles (HEV) and electric vehicles (EV).[2-4] Generally, the performance of the LIBs is mainly limited by the deterioration in microstructure of the electrode materials.[5-8] The electrode materials with a wide variety of nanostructure have promising future in increasing energy density and rate capability due to their large surface area increasing the contact area between electrode and electrolyte, short path lengths for lithium ion diffusion and electron transport, enhanced ionic and electronic conductivity, and improved mechanical strength and structural integrity.[9-15] Recently, there are few reports on two-dimensional (2D) nanostructured vanadium oxide electrode material for LIBs.[16] 2D nanosheets materials, with large active surface area and short transport path for lithium ions insertion/extraction, can exhibit more effective surface and better sensible distribution than one-dimensional (1D) nanostructure, which are ideal frameworks for fast lithium storage.[17,18]

Vanadium oxide with a typically layered structure has been widely researched and considered as a promising cathode for LIBs.[19-22] However, the ionic and electronic conductivities of vanadium oxide materials need to be improved to meet the requirement of its application. Carbon nanotubes (CNTs) have high aspect ratio and good electronic transport properties, which can offer high conductivity, good interfacial contact, and stability strucutre.[23] Hence, various approaches have been developed to design low-dimensional nanocomposites which can combine the advantages of vanadium oxide and CNTs for better performance.[24,25] The carbon tube-in-tube nanostructure was fabricated by a so-gel method with V_2O_5 anchored on CNTs.[26,27] The hydrothermal method has been used to synthesize a network architecture nanocomposites with V_2O_5 nanotubes or nanowires crosslink with CNTs to form a robust and high performance electrode.[28,29] A three-dimensional nanoarchitecture consisting of mesoporous V_2O_5 and CNTs was synthesized via an aerosol-spray drying process.[30,31] The chemical vapour deposition (CVD) is another effective way to prepare V_2O_5/CNTs nanocompsoites.[32] However, most of these approaches cannot form 2D nanostructure, or require expensive precursors and facilities.

In this paper, the V_2O_5 nanosheets/CNTs nanocomposite has been fabricated by a simple, facile and green vacuum freeze-drying method. The V_2O_5 nanosheets and CNTs build a three-dimensional (3D) interpenetrating network. The 2D V_2O_5 nanosheets provide high lithium storage capacity with large active surface and shorten lithium diffusion length while the

CNTs provide fast electron transport pathways. The interpenetrating network can not only create interconnected channels for effective ion transport, but also provide excellent mechanical property for high rate lithium storage performance. Thus, the V_2O_5 nanosheets/CNTs nanocomposite displays superior electrochemical performance with large reversible capacity, perfect structure stability, high coulombic efficiency and great cyclic property at large current density, making it a potential fast charge/discharge cathode material in LIBs.

Results and discussion

The phase of the nanocomposite transferred from $V_2O_5{\cdot}1.6H_2O$ xerogel (Fig. S1†) to orthorhombic V_2O_5 (Fig. 1(a)) when it was followed a heating treatment. Fig. 1(a) shows the XRD pattern of the V_2O_5 nanosheets/CNTs nanocomposite annealed at 350 ℃ for 2 hours in N_2 atmosphere. All the diffraction peaks signed (♦) can be indexed to an orthorhombic phase V_2O_5 (JCPDS card No. 01-076-1803). A strong and broad FWHM diffraction peak at 2θ=26.6 ° is obviously due to the (002) diffraction of graphite from the CNTs. The XRD diffraction peak positions of the V_2O_5 nanosheets/CNTs nanocomposites show no significant change as the addition ratio of CNTs increases from 0 to 20 wt.% (Fig. S2†).

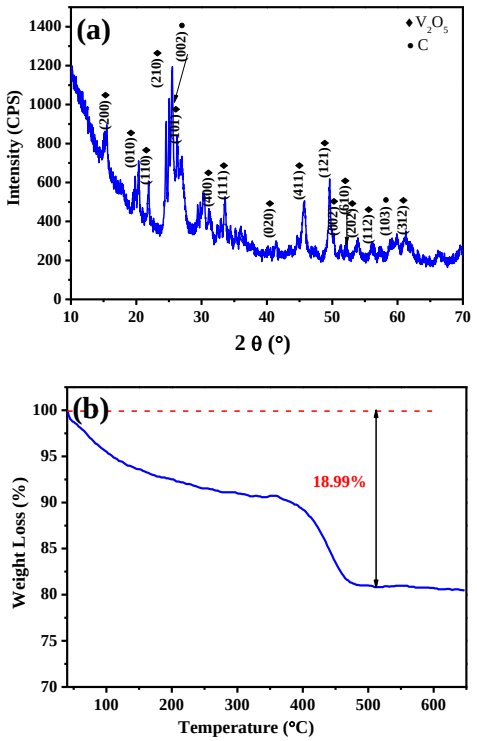

Fig. 1 (a) XRD pattern of the V_2O_5 nanosheets/CNTs nanocomposite. (b) TG curve of the V_2O_5 nanosheets/CNTs nanocomposite.

Thermogravimetric (TG) curve of the V_2O_5 nanosheets/CNTs nanocomposite under air atmosphere is illustrated in Fig. 1(b). It can be observed that 18.99% weight loss in 40-500 ℃ is due to the removal of adsorbed and constitutional water and decomposition of CNTs in air. The weight loss is approach the addition percentage of the CNTs (20.0 wt%) in the original synthesis process.

The formation of the V_2O_5 nanosheets/CNTs nanocomposite is further investigated by X-ray photoelectron spectroscopy (XPS). Fig. 2(a) shows survey spectrum for V_2O_5 nanosheets/CNTs nanocomposite. The corresponding peaks confirm that the vanadium, carbon and oxygen elements are detected. The core level binding energies of $V2p_{3/2}$ spectrum (Fig. 2(b)) can be divided into two peaks at 517.40 eV and 515.80 eV, which are ascribed to V^{5+} and V^{4+} species, respectively . The core level binding energies of C1s spectrum in Fig. 2(c) can be divided into three peaks appearing at 284.64, 286.54, and 288.70 eV.[33] The main peak at 284.64 eV originates from sp^2-hybridized graphite-like carbon atoms in CNTs which bound to hydrogen atoms. Peaks with higher binding energies located at 286.54, and 288.77 eV are considered to be originated from -C-O and -C=O bonding, respectively, due to a positive charge on a carbon atom induced the electronegative oxygen atoms.[34] As shown in Fig. 2(d), the O1s spectrum is broad and asymmetric, which could be deconvoluted into three peaks indicating the existence of three different oxygen species. The peak located at 530.20 eV can be assigned as oxygen in V_2O_5. In addition, the peaks at 531.40 and 533.0 eV are attributed to OH groups and H_2O molecules, respectively.[27]

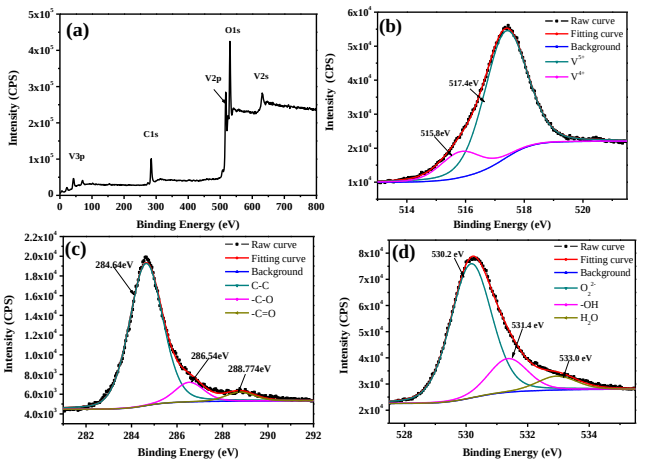

Fig. 2. XPS observation of the V_2O_5 nanosheets/CNTs nanocomposite: (a) survey spectrum; (b) $V2p_{3/2}$ spectrum; (c) C1s spectrum; (d) O1s spectrum.

Fig. 3 presents the FESEM and TEM images of V_2O_5 nanosheets/CNTs nanocomposite. It can be seen that V_2O_5 nanosheets and CNTs build a uniform and homogeneous macro-morphology (Fig. 3(a)). The CNTs act as "supporting-steel like" architecture and the V_2O_5 nanosheets are anchored on the CNTs. They corporately form a highly porous structure (Fig. 3(b)). The TEM images (Fig. 3(d) and (e)) confirm that the V_2O_5 nanosheets and CNTs form of a 3D interpenetrating network structure. Furthermore, the HRTEM image in Fig. 3(f) exhibits the lattice fringes of the nanocomposite, where the

lattice plane with d spacing of 0.3345 nm is corresponded to the (002) plane of CNTs. The lattice planes with d spacing of 0.3497 and 0.3313 nm can be indexed to the (210) and (101) planes of orthorhombic V_2O_5, respectively. It is generally acknowledged that most of nanosheets are easily overlapped and get bunched up to form bigger bulk due to the Ostwald ripening process, attributing to the decrease of actually active surface and capacity loss for electrode materials.[22] In this work, V_2O_5 nanosheets are anchored on the surface of CNTs without overlap phenomenon. As the addition ratio of CNTs increases from 0 to 20 wt.%, the morphology of the V_2O_5 nanosheets/CNTs nanocomposites becomes more homogenous and the size of the V_2O_5 nanosheets becomes smaller (Fig. S3 and 4†).

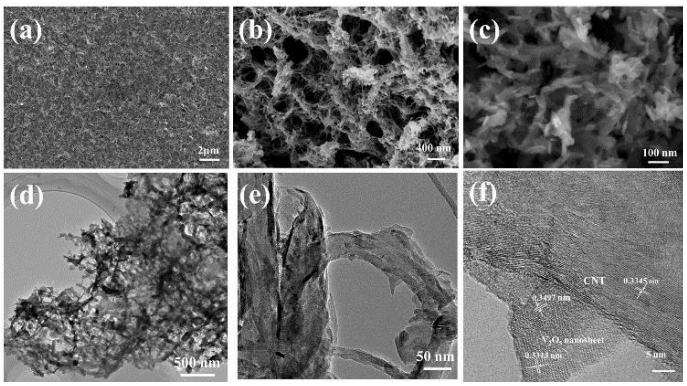

Fig. 3 The morphology observation of the V_2O_5 nanosheets/CNTs nanocomposite. (a), (b) Low- and (c) high-magnification FESEM images; (d), (e) TEM and (f) HRTEM images.

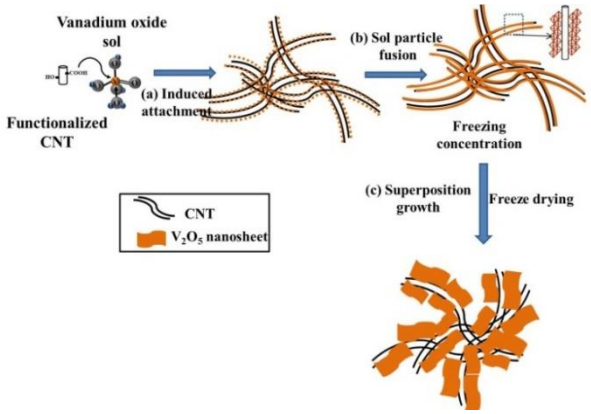

Fig. 4 Schematic illustration of the formation of the V_2O_5 nanosheets/CNTs nanocomposite.

The formation mechanism of the 1D and 2D mixed nanostructure can be illustrated as Fig. 4. The functional groups on the CNTs surface serve as reaction centres. As the CNTs add into the vanadium oxide sol, the vanadium oxy-tripropoxides attach to the CNTs surface with the electrostatic interaction of functional groups on the CNTs surface.[35] During freeze-drying process, the hydrates in V_2O_5 sol are frozen and removed out. In the meantime, the vanadium oxy-trihydroxides condensate and develop into V_2O_5 nanosheets on the surface of CNTs. The Brunauer Emmett-Teller (BET) specific surface area has been estimated to be 30.0 m^2g^{-1}.

Cyclic voltammetry (CV) and galvanostatic charge/discharge measurements were carried out to investigate the electrochemical behaviors of the samples. Fig. 5(a) shows the CV curves of the V_2O_5 nanosheets/CNTs nanocomposite between the potential of 2.0-4.0 V (*vs.* Li/Li^+) at a scan rate of 0.5 mV s^{-1} after different cycles. During the lithium ions intercalation process, the phase of V_2O_5 is orderly transferred: α-$Li_xV_2O_5$ phase ($x<0.1$), ε-$Li_xV_2O_5$ phase ($0.35<x<0.7$), δ-$Li_xV_2O_5$ phase ($0.9<x<1$), and then γ-$Li_xV_2O_5$ phase ($1<x<2$).[36,37] The α/ε and ε/δ phase transition processes are completely reversible because the phase structures of ε-$Li_xV_2O_5$ and δ-$Li_xV_2O_5$ are very similar to that of the pristine V_2O_5. While the δ/γ transition process has a slight irreversibility caused by puckering of the V_2O_5 layers when more than 1.0 mol Li ions insert into one mol V_2O_5.[30,38] In the first cycle, the three reduction peaks located at 3.37, 2.68, and 2.41 V are attributed to phase transition of α/ε, ε/δ, and δ/γ, respectively. The oxidation peaks located at 2.30, 2.78, and 3.28 V are corresponding to the backward transition of phases. An additional cathodic peak appeared at the potential of 2.17 V can be attributed to the irreversible transition of γ/ω process, but it disappears after several cycles. At the 100th cycle, the intensities and positions of the three pairs of cathodic peaks (located at 3.32, 2.73, and 2.45 V) and anodic peaks (located at 2.25, 2.71 and 3.29 V) weaken and shift compared to the first cycle. This phenomenon indicates an electrochemical polarization process during the battery cycles. Moreover, the CV curve areas in the first cycle between 3.2 and 4.0 V (corresponding to the phase transition of α/ε and ε/δ) are almost the same compared to the 100th cycle. It is assumed that the main capacity loss of the nanocomposites occurs in the phase transitions of ε/δ and δ/γ during the lithium ion insertion and extraction process.

Fig. 5(b) presents the galvanostatic charge-discharge curves of the V_2O_5 nanosheets/CNTs nanocomposites at various current densities between the potential of 2.0-4.0 V (*vs.* Li/Li^+) at room temperature. It can be observed that the nanocomposites exhibit obvious reversible plateau regions at all current densities. The charge/discharge curves can be divided into three stages according to the different slopes, appearing at around of 3.15/3.25, 2.6/2.75, and 2.3/2.25 V. These voltage states are agreeing well with the redox peaks as shown in the CV curves. As the current density increases, the discharge voltage decreases and the charge voltage increases due to the effect of increasing electrochemical polarization. The nanocomposite with open nanoporous can provide short path for lithium insertion and can absorb electrolyte, leading to reduce electrode polarization.

Fig. 5(c) exhibits the cycling performance of the V_2O_5 nanosheets/CNTs nanocomposite electrodes at different current densities in the potential of 2.0-4.0 V (*vs.* Li/Li^+) at room temperature. It is noticeable that with the increases of current density, the specific capacity of V_2O_5 nanosheets/CNTs

nanocomposite becomes more stable. As listed in Table 1, at the current density of 0.1 Ag^{-1}, the initial discharge specific capacity is 245.8 $mAhg^{-1}$ and the capacity remains 103.6 $mAhg^{-1}$ after 100 cycles. When the current density reaches 5.0 Ag^{-1}, the initial discharge specific capacity is 130 mAh g^{-1} and the capacity maintains 100.1 $mAhg^{-1}$ after 100 cycles. As the current densities increases from 0.1 to 5.0 Ag^{-1}, the 100th reversible capacity retention rates of the V_2O_5 nanosheets/CNTs nanocomposite electrodes are 41.9 %, 49.1 %, 60.6 %, 65.0 %,and 76.6 %, respectively, compared to the first capacity. In addition, the average capacity fading rate is 0.83 %, 0.69 %, 0.49 %, 0.32 %, and 0.17 % per cycle at the current densities of 0.1, 0.5, 1.0, 2.0, and 5.0 Ag^{-1}, respectively.

Fig. S5† shows the specific discharge capacities *vs.* cycle number of the V_2O_5 nanosheets/CNTs nanocomposite with different CNTs ratio at the current densities of 0.1, 0.5, and 1 Ag^{-1}. When the discharge current density at 0.1 Ag^{-1}, the V_2O_5 nanosheets/CNTs nanocomposite with low CNTs ratio performs higher initial specific capacity but poor cycle stability. While as the discharge current density increases to 1 Ag^{-1}, the results show a contrary phenomenon. One reason for this phenomenon is that the V_2O_5 nanosheets generate a deep lithium ions insertion process at low current density but a slight lithium ions insertion process at high current density. On the other hand, calculating method for the specific capacity is based on the total mass of V_2O_5 nanosheets/CNTs. It may cause a relative decrease for active materials at high CNTs ratio.

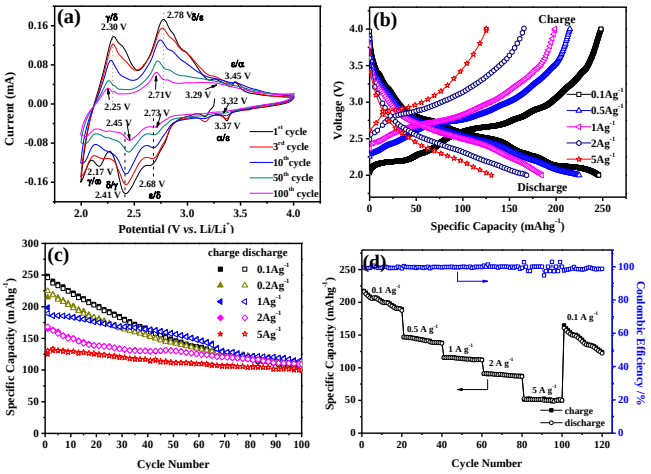

Fig. 5 Electrochemical performance of the V_2O_5 nanosheets/CNTs nanocomposite electrodes. (a) CV curves for different cycles at a scan of 0.5 mVs^{-1}; (b) charge/discharge curves; (c) cycling performance; (d) rate capability at various current densities.

Table 1 The discharge capacities of the V_2O_5 nanosheets/CNTs nanocomposites at different current densities.

Current density/ Ag^{-1}	Initial discharge capacity/ $mAhg^{-1}$	100th discharge capacity/ $mAhg^{-1}$	Capacity retention rate after 100 cycles/ %	Average capacity fading rate/ %
0.1	245.8	103.6	41.9	0.83
0.5	224.8	110.4	49.1	0.69
1	189.3	114.7	60.6	0.49
2	168.4	109.5	65.0	0.32
5	130.7	100.1	76.6	0.17

Table 2 EIS fitting kinetic parameters of the V_2O_5 nanosheets/CNTs nanocomposite electrode.

Cycle number	R_s / Ω	R_f/ Ω	R_{ct} / Ω	σ_ω/ Ω $cms^{-1/2}$
1st cycle	3.75	9.91	311.0	242.92
10th cycle	2.69	67.8	262.0	258.93
50th cycle	2.41	70.8	302.0	246.75
100th cycle	2.96	81.4	368.0	312.02

.

It can be seen that the V_2O_5 nanosheets/CNTs nanocomposite electrode shows high initial discharge capacity but low capacity stability at low current density, which caused by the irreversible transition phase γ-V_2O_5. At large current density, the electrochemical performances of the V_2O_5 nanosheets/CNTs nanocomposite electrode can be attributed to their unique

architecture as follows: (1) V_2O_5 nanosheets with short path length allow maximum lithium ion diffusion and electron transport during cycles.[18] (2) Plenty of active sites for lithium ions insertion/extraction are caused by the large specific surface of the nanocomposite. (3) The nanoporous architecture of the V_2O_5 nanosheets/CNTs nanocomposite can release the volume swells to stabilize the electrode.[39]

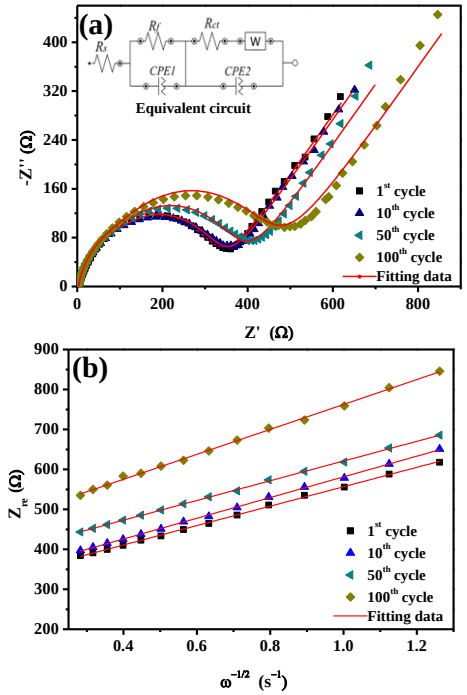

Fig. 6 EIS results of the V_2O_5 nanosheets/CNTs nanocomposite electrode in the coin cell after cycling at current density of 0.5 Ag^{-1}: (a) Nyquist plots after different cycles. Inset shows the equivalent circuit corresponding to the Nyquist plots. (b) The relationship between Z_{re} and $\omega^{-1/2}$ at low frequencies.

Fig. 5(d) shows rate capability of the V_2O_5 nanosheets/CNTs nanocomposite (20 cycles at each rate) at the current densities of 0.1, 0.5, 1.0, 2.0, and 5.0 Ag^{-1}, respectively. The initial specific capacity of the nanocomposite remains at 216.3 $mAhg^{-1}$ at the current density of 0.1 Ag^{-1}. When the current densities reach 0.5, 1.0, 2.0, and 5.0 Ag^{-1}, the capacities of the electrode can still hold 147.0, 115.4, 91.1, and 52.3 $mAhg^{-1}$, respectively. The specific capacity recovers to 160.7 $mAhg^{-1}$ after returning to the current density of 0.1 Ag^{-1}. In addition, the Coulombic efficiency (as shown in Fig. 5(d)) is above 99.0 %, even at the large current density. These results demonstrate a high rate capability of the V_2O_5 nanosheets/CNTs nanocomposite.

To further understand the interfacial transport kinetics for the V_2O_5 nanosheets/CNTs nanocomposite electrode, the EIS measurements are carried out after different cycles at the current density of 0.5 Ag^{-1}. The plots consist of a depressed semicircle at high-to-middle frequency regions and an inclined line within the low frequency region. In order to obtain the quantitative analysis of the Nyquist plots, an equivalent circuit for this model is shown in the inset of Fig. 6(a). In the equivalent circuit, R_s represents the total resistance of electrolyte, electrode and separator. R_f and CPE1 refer to the resistance of solid-electrolyte interface (SEI) film and capacitance formed on the electrode, corresponding to the first semicircle at high frequency region. Similarly, R_{ct} and CPE2 are designated to the charge transfer resistance and double-layer capacitance, corresponding to the second semicircle at medium frequency region. W is the Warburg impedance or so-called Warburg diffusion related to the diffusion of lithium ions into the active materials, corresponding to the inclined line at low frequency region.[40] Fig. 6(b) presents the linear relationship between the impedance impedance modulus (Z_{re}) and the inverse of the square root of angular frequency ($\omega^{-1/2}$) in the low frequency region for the V_2O_5 nanosheets/CNTs nanocomposites electrode after different cycles. The slop of the straight line in Fig. 6(b) presents the Warburg impedance coefficient (σ_ω). Afterwards, the squared value of σ_ω is inversely proportional to the Li^+ diffusion coefficient ($D_{Li} \propto 1/\sigma_\omega^2$).[41,42] Thus, we can investigate the electrode change after several cycles by using the σ_ω values to indirectly evaluate the Li^+ diffusion efficiency.

Table 2 exhibits the kinetic parameters of the V_2O_5 nanosheets/CNTs nanocomposite electrode. The values of R_s are quite small and show no significant difference for the electrode with different cycles. The value of R_f is 9.91 Ω after 1st cycle, and it increases rapidly to 67.8 Ω after the 10th cycle, then the R_f increases slightly to 70.8 Ω after the 50th cycle. These changes are corresponding to the formation and development of the SEI between the electrode and electrolyte. It has been commonly known that the formation and development of the SEI layer in initial cycle is helpful for lithium ions insertion and extraction. The SEI layer can act as a transport pathway for lithium ions that keeps direct contact and contributes to interaction between electrode reactants and the electrolyte. Therefore, the values of R_{ct} decrease from 311.0 to 262.0 Ω when the cycles increase from 1 to 10. The lower R_{ct} reflects the fact that charge transfer is facilitated since the SEI layer forms on the surfaces of the electrode. It is believed that the electrode undergoes a physical disassembly reaction on the surface of V_2O_5 nanosheets/CNTs nanocomposite after the initial several cycles. As the cycle number increases from 10 to100, the R_{ct} increases from 262.0 to 368.0 Ω. It means that the SEI layer breaks down and reforms continuously upon cycling. In addition, the values of σ_ω can be used to evaluate the Li^+ diffusion coefficient indirectly. The lower σ_ω is, the faster Li^+ diffusion is. As it can be seen in Table 2, the values of σ_ω for the V_2O_5 nanosheets/CNTs nanocomposite electrode show no significant change after the 50th cycle, indicating steady efficiently Li^+ ions diffusion. When the cycle number increases to the 100, the σ_ω increases gradually indicating the slow Li^+ ions diffusion. It may be caused by the electrolyte discomposing and irreversibly insertion/extraction during the cycling period.

Conclusions

In summary, the V_2O_5 nanosheets/CNTs nanocomposite was fabricated by facile freezing-drying method. The CNTs act as supporting bond architecture, and the V_2O_5 nanosheets attach on the surface of CNTs. They build stable interpenetrating network. The unique porous structure including large specific surface and short lithium diffusion path of V_2O_5 nanosheets and high conductivity CNTs leads to the superior electrochemical performance, especially in cyclability and structure stability. Even at the current density of 5.0 Ag^{-1} after 100 cycles, the V_2O_5 nanosheets/CNTs nanocomposite could deliver a capacity of 100.1 $mAhg^{-1}$ with average capacity fading rate of 0.17 % per cycle.

Experimental Section

Synthesis of the functionalized CNTs. CNTs were purchased from Shenzhen Nanotech Port Co., Ltd. (>97% purity, length 5-15 μm, outer diameter 20-40 nm, special surface area 90-120 m^2g^{-1}), and then they were pretreated by mix acid. Briefly, pristine CNTs were added into a 1:3 (v/v) mixture concentrated of HNO_3/H_2SO_4. Then, the mixture was ultrasonic for 7 h. After that, the mixture was diluted with deionized water, filtered, and re-dispersed in water. This process was repeated until the pH of the filtrate was around neutral. Finally, functionalized CNTs were dried and milled.

Synthesis of the vanadium oxide sol. In a typical synthesis, V_2O_5 powders (99.0%, Sinopharm Chemical Reagent Co., Ltd.) were added to distilled water and stirred to form a light yellow slurry solution. Then, H_2O_2 (30.0 wt.% in H_2O, Sinopharm Chemical Reagent Co., Ltd.) was added drop wise to the slurry solution and stirred for 2 h to form an orange solution. The resulting orange solution was put static for 24h to form a vanadium oxide sol.

Synthesis of the V_2O_5 nanosheets/CNTs nanocomposite. The prepared functionalized CNTs were added into V_2O_5 sol with a CNTs/V_2O_5 concentration of 20.0 wt.%. After a vigorous stirring and ultrasonic process, the mixture became suspension solution. Then the suspension was pre-frozen in a freeze refrigerator at -60 ℃ for one day and freeze-dried under vacuum at -40 ℃ for two days. After drying the samples were annealed in nitrogen atmosphere at 350 ℃ for two hours.

Material characterization. The crystallographic structures of the samples were characterized by a powder X-ray diffraction system (XRD, PANalytical, Netherlands) equipped with Cu Kα radiation (λ=1.5418 Å). The morphologies of the samples were observed by the field emission scanning electron microscopy (FESEM, JSM-6700F, JEOL, Tokyo, Japan) and transmission electron microscopy (TEM, JEOL, JEM-2100F, Tokyo, Japan). X-ray photoelectron spectroscopy (XPS) measurements were acquired using a VG Multilab 2000 with Al Kα as the radiation source. All XPS spectra were corrected by the C1s line at 284.8 eV.

Electrochemical measurements. The electrochemical properties were investigated in CR 2035 coin-type cell with a metallic lithium foil as the anode electrode. The electrolyte was a 1.0 M $LiPF_6$ dissolved in ethylene carbonate (EC)/dimethyl carbonate (DMC) (1:1 volume ratio). And the separator was a polypropylene micro-porous film (Cellgard 2300). The cathodes consist of the V_2O_5/CNTs nanocomposite, mixed with carbon black and poly(vinyldifluoride) (PVDF) at a weight ratio of 80: 15: 5. The cells were assembled in an argon-filled glove box at room temperature. For galvanostatic charge-discharge test, first constant discharge and discharge/charge cycling (DC) analysis were performed by the battery test system (CT-2008W). The CV and EIS measurements were carried out by using an Autolab Potentiostat 30 system. The frequency of EIS test ranges from 0.1 Hz to 100 kHz at the open circuit voltage (OCV) with 10 mV amplitude voltage.

Acknowledgements

This work was financially supported by International Science and Technology Cooperation Program of China (2013DFR50710), National Natural Science Foundation of China (51472189) and the Fundamental Research Funds for the Central Universities (20131049701001, 145101008).

Notes and References

[a]State Key Laboratory of Advanced Technology for Materials Synthesis and Processing, School of Materials Science and Engineering, Wuhan University of Technology, Wuhan 430070, P. R. China, Email: chenw@whut.edu.cn.

[b]Institute of Solid State Chemistry, Ural Branch of the Russian Academy of Science, Ekaterinburg 620990, Russian Federation.

[#]This author contributed equally to this study and share first authorship. All authors discussed the results and commented on the manuscript. The authors declare no competing financial interest.

1 J.B. Goodenough and K.S. Park, *J. Am. Chem. Soc.*,2013, **135,** 1167-1176.
2 B. Xu, D. Qian, Z. Wang and Y.S. Meng, *Mater. Sci. Eng. R*, 2012, **73,** 51-65.
3 J.B. Goodenough and Y. Kim, *J. Power Sources*, 2011, **196,** 6688-6694.
4 N.-S. Choi, Z. Chen, S.A. Freunberger, X. Ji, Y.-K. Sun, K. Amine, G. Yushin, L.F. Nazar, J. Cho and P.G. Bruce, *Angew. Chem. Int. Ed.*, 2012, **51,** 2-23.
5 Y.N. Xia, P.D. Yang, Y.G. Sun, Y.Y. Wu, B. Mayer and B. Gates, *Adv. Mater.*, 2003, **15,** 353-389.
6 M.S. Whittingham, *Chem. Rev.*, 2004, **104**, 4271-4302.
7 H.-K. Song, K.T. Lee, M.G. Kim, L.F. Nazar and J. Cho, *Adv. Funct. Mater.*, 2010, **20,** 3818-3834.
8 A.L. Mohana Reddy, S.R. Gowda, M.M. Shaijumon and P.M. Ajayan, *Adv. Mater.*, 2012, **24**, 5045-5064.
9 M.-K. Song, S. Park, F.M. Alamgir, J. Cho and M. Liu, *Mater. Sci. Eng. R*, 2011, **72**, 203-252.
10 R. Pitchai, V. Thavasi, S.G. Mhaisalkar and S. Ramakrishna, *J. Mater. Chem.*, 2011, **21**, 11040-11051.
11 M.G. Kim and J. Cho, *Adv. Funct. Mater.*, 2009, **19**, 1497-1514.
12 S.J. Dillon and K. Sun, Curr. Opin. *Solid State Mater. Sci.*, 2012, **16**, 153-162.
13 X. Chen, C. Li, M. Grätzel, R. Kostecki and S.S. Mao, *Chem. Soc. Rev.*, 2012, **41**, 7909-7937.
14 Y.L. Cheah, R. von Hagen, V. Aravindan, R. Fiz, S. Mathur and S. Madhavi, *Nano Energy*, 2013, **2**, 57-64.
15 P.G. Bruce, B. Scrosati and J.-M. Tarascon, *Angew. Chem. Int. Ed.*, 2008, **47**, 2930-2946.

16 Y. Li, J. Yao, E. Uchaker, J. Yang, Y. Huang, M. Zhang and G. Cao, *Adv. Energy Mater.*, 2013, **3**, 1171-1175.
17 M. Naguib, O. Mashtalir, J. Carle, V. Presser, J. Lu, L. Hultman, Y. Gogotsi and M.W. Barsoum, *ACS Nano*, 2012, **6**, 1322-1331.
18 J. Liu and X.W. Liu, *Adv. Mater.*, 2012, **24**, 4097-4111.6 G. Silversmit, D. Depla, H. Poelman, G.B. Marin and R. De Gryse, *J. Electron. Spectrosc. Relat. Phenom.*, 2004, **135**, 167-175
19 X. Zhou, G. Wu, G. Gao, J. Wang, H. Yang, J. Wu, J. Shen, B. Zhou and Z. Zhang, *J. Phys. Chem. C*, 2012, **116**, 21685-21692.
20 Y. Zhang, C. Chen, W. Wu, F. Niu, X. Liu, Y. Zhong, Y. Cao, X. Liu and C. Huang, *Ceram. Int.*, 2013, **39**, 129-141.
21 J. Shao, X. Li, Z. Wan, L. Zhang, Y. Ding, L. Zhang, Q. Qu and H. Zheng, *ACS Appl. Mater. Interf.*, 2013, **5**, 7671-7675.
22 J. Livage, *Materal*, 2010, **3**, 4175-4195.
23 M. Zhi, C. Xiang, J. Li, M. Li and N. Wu, *Nanoscale*, 2013, **5**, 72-88.
24 X. Zhou, G. Wu, G. Gao, C. Cui, H. Yang, J. Shen, B. Zhou and Z. Zhang, *Electrochim. Acta*, 2012, **74**, 32-38.
25 Q. Zhu, Z. Li, S. Huang, X. Zhang, W. Chen and G.S. Zakharova, *Electrochim. Acta*, 2012, **81**, 25-30.
26 Y.-S. Hu, X. Liu, J.-O. Müller, R. Schlögl, J. Maier and D.S. Su, *Angew. Chem. Int. Ed.*, 2008. **48**, 210-214.
27 M. Sathiya, A.S. Prakash, K. Ramesha, J.M. Tarascon and A.K. Shukla, *J. Am. Chem. Soc.*, 2011, **133**, 16291-16299.
28 X. Jia, Z. Chen, A. Suwarnasarn, L. Rice, X. Wang, H. Sohn, Q. Zhang, B.M. Wu, F. Wei, and Y. Lu, *Energy Environ. Sci.*, 2012, **5**, 6845-6849.
29 R. Yu, C. Zhang, Q. Meng, Z. Chen, H. Liu and Z. Guo, *ACS Appl. Mater. Interf.*, 2013, **5**, 12394-12399.
30 Z. Cao and B. Wei, *Nano Energy*, 2013, **2**, 481-490.
31 Y.L. Cheah, R. von Hagen, V. Aravindan, R. Fiz, S. Mathur and S. Madhavi, *Nano Energy*, 2013, **2**, 57-64.
32 X. Jia, L. Zhang, R. Zhang, Y. Lu and F. Wei, *RSC Adv.*, 2014, **4**, 21018-21022.
33 G. Silversmit, D. Depla, H. Poelman, G.B. Marin and R. De Gryse, *J. Electron. Spectrosc. Relat. Phenom.*, 2004, 135, 167-175.
34 G. Zhang, S. Sun, D. Yang, J.-P. Dodelet and E. Sacher, *Carbon*, 2008, **46**, 196-205.
35 Z. Li, X. Zhang, J. Xu, S. Huang, Q. Zhu, W. Chen and G.S. Zakharova, *J. Mater. Res.*, 2013, **28**, 627-634.
36 P. Rozier, J.M. Savariault and J. Galy, *Solid State Ionics*, 1997, **98**, 133-144.
37 R. Baddour-Hadjean, A. Marzouk and J.P. Pereira-Ramos, *J. Raman Spectrosc.*, 2012, **43**, 153-160.
38 C. Leger, S. Bach, P. Soudan and J.P. Pereira-Ramos, *J. Electrochem. Soc.*, 2005, **152**, A236-A241.
39 J.J. Yu, J. Yang, W.B. Nie, Z.H. Li, E.H. Liu, G.T. Lei and Q.Z. Xiao, *Electrochim. Acta*, 2013, **89**, 292-299.
40 D.A. Semenenko, T.L. Kulova, A.M. Skundin, D.M. Itkis, E.A. Pomerantseva, E.A. Goodilin and Y.D. Tretyakov, *Mendeleev Commun.*, 2010, **20**, 12-14.
41 Y. Cui, X. Zhao and R. Guo, *Electrochim. Acta*, 2010, **55**, 922-926.
42 X. Zhou, G. Wu, J. Wu, H. Yang, J. Wang, G. Gao, R. Cai and Q. Yan, *J. Mater. Chem. A*, 2013, **1**, 15459-15468.